Post-buckling behavior and collapse of Double-Double composite single stringer specimens

Vescovini, Alessandro; Li, Carina Xiaochen; Paz Mendez, Javier; Jin, Bo Cheng; Manes, Andrea; Bisagni, Chiara

DOI
10.1016/j.compstruct.2023.117699

Publication date
2024

Document Version
Final published version

Published in
Composite Structures

Composite Structures 327 (2024) 117699

Contents lists available at ScienceDirect

Composite Structures

journal homepage: www.elsevier.com/locate/compstruct

Post-buckling behavior and collapse of Double-Double composite single stringer specimens

Alessandro Vescovini [a,*], Carina Xiaochen Li [b], Javier Paz Mendez [c,d], Bo Cheng Jin [e], Andrea Manes [a], Chiara Bisagni [c,f]

[a] Department of Mechanical Engineering, Politecnico di Milano, Milan, Italy
[b] Department of Chemical Engineering and Materials Science, University of Southern California, Los Angeles, CA, USA
[c] Faculty of Aerospace Engineering, Delft University of Technology, Delft, The Netherlands
[d] Aerospace Systems and Transport Research Group, Universidad Rey Juan Carlos, Madrid, Spain
[e] Department of Aerospace and Mechanical Engineering, University of Southern California, Los Angeles, CA, USA
[f] Department of Aerospace Science and Technology, Politecnico di Milano, Milan, Italy

ARTICLE INFO

Keywords:
Post-buckling
Double-Double (DD)
Experimental tests
Finite element analysis

ABSTRACT

This paper presents the work on six single-stringer specimens manufactured using the card-sliding technique with non-crimp fabrics and adopting a Double-Double (DD) stacking sequence. These specimens, representative of sub-structure level components, are used to investigate post-buckling and failure in aerospace structures. Two specimens maintain a constant thickness cross-section, while four are tapered, two of which incorporate a Teflon insert in the stringer flange. All specimens are tested under compression loading conditions, inducing skin buckling, skin-stringer separation, and eventual collapse. Numerical simulations are validated by experimental results and serve to analyze the specimens behavior and the failure mode. The load versus displacement curves of both experimental tests and Finite Element Method (FEM) analyses are compared, along with the out-of-plane displacement field. Subsequently, the observed failure modes are discussed, focusing on the various mechanisms that occurred and considering the impact of flanges and stiffener tapering. Both the FEM simulations and experimental tests demonstrate good agreement, with the flanges tapering revealing notable results. This offers promising evidence of a viable solution to optimize aeronautical structures and enhance resistance to skin-stringer separation.

1. Introduction

Composite materials, due to their high strength-to-weight ratio and durability, are increasingly gaining popularity in the aerospace industry. However, these materials can be susceptible to various types of failure modes, such as delamination, fiber breakage, and matrix cracking, thereby compromising structural integrity. Compression loading proves to be a critical factor in determining the strength and stability of aerospace structures. One of the challenges posed by compression loading is the potential for buckling, which can significantly deteriorate the strength and stability of a structure. Thin-walled structures tend to buckle when subjected to compression and shear loads, and they are typically designed to avoid this condition. However, there exists a potential opportunity for substantial weight reduction by enabling primary structures to operate in the post-buckling field below ultimate loads. Considering that failure commonly occurs after buckling, realizing this potential necessitates a comprehensive understanding of the structural response, and the design of stronger structures capable of sustaining larger deformation before collapsing. To understand the buckling behavior of aeronautical structures, specimens are utilized to simplify the model and provide insight into post-buckling structural behavior, as failures often occurs after buckling [1].

Several researchers have conducted experiments focused on buckling and post-buckling behavior. Zimmermann et al. [2] studied curved composite panels with stiffeners subjected to axial compression. Similarly, Degenhardt et al. [3] designed an experiment with the object of producing a large post-buckling region and early onset of degradation. Abramovich et al. [4] on the other hand, performed buckling tests on stiffened composite laminated panels under combined shear-axial compression. In a later study, Abramovich and Weller [5] conducted

* Corresponding author.
E-mail address: alessandro.vescovini@polimi.it (A. Vescovini).

https://doi.org/10.1016/j.compstruct.2023.117699
Received 26 July 2023; Received in revised form 8 September 2023; Accepted 2 November 2023
Available online 4 November 2023

repeated buckling and post-buckling tests on laminated stringer stiffened composite panels, both with and without damage.

Most recent research has concentrated on skin-stringer separation in aircraft structures using single-stringer specimens with an omega stiffener. Bisagni et al. [6,7] developed Single-Stringer Compression Specimens (SSCS) through finite element analysis of multi-stringer panels to predict the desired buckling and failure behavior of the specimens. Vescovini et al. [8] further investigated SSCS numerically using a simplified model and a global/local damage analysis. This allowed for an efficient investigation of the effect of structural design and numerical parameters on buckling, post-buckling, and failure behavior. In terms of damage tolerance, Dávila and Bisagni [9] conducted a combined experimental and numerical investigation, employing the Virtual Crack Closure Technique (VCCT) in the numerical analysis to model skin-stringer separation. Kootte and Bisagni [10] also proposed another method of investigating skin-stringer separation by applying out-of-plane displacement directly to the skin.

The composite structures studied in all these papers share a common feature: they are manufactured with balanced symmetric stacking sequence of carbon fiber plies oriented along 0°, 90° and ±45°, i.e., the quasi-isotropic stacking sequence, following well-established industry practices. However, recent years have seen the proposal of a novel layup method by Prof. S. W. Tsai. This method involves repeating four plies, i.e., $[\pm\phi/\pm\psi]$, or two plies, i.e., $[\pm\phi]$ sub-laminate, referred to as Double-Double (DD) or Single-Double (SD) stacking sequences, respectively [11,12]. By using this stacking sequence, the composite material becomes balanced, simplifying the manufacturing process. Additionally, the angle of the repetitive unit can be continuously varied depending on stiffness and strength requirements, and plies can be dropped simply by removing one repetitive unit. This avoids impacting in-plane stiffness or introducing abrupt changes in thickness. Recent efforts have shown how Quad composite stacking sequence can be converted to DD, achieving lower weight without compromising strength, possibly relieving interlaminar stresses by easing homogenization and reducing the angle difference between adjacent plies [13–16].

Non-crimp fabrics (NCFs), consisting of stitched uni-directional (UD) thin-plies, have emerged in the past decade and are a viable alternative to traditional UD prepreg tapes and crimp textiles. NCFs represent an interesting solution for DD composites design as a single fabric constitutes half of the repetitive unit of a DD stacking sequence, further simplifying the manufacturing process. Despite the presence of yarns slightly reducing the in-plane elastic and strength properties, an effect mitigated in thin plies, NCFs exhibit performance comparable to UD prepreg laminates [17–19]. These fabrics cater to the increasing demand for enhanced damage resistance and tolerance, improved out-of-plane properties, and lower manufacturing costs.

So far, coupon level investigations are found in the literature on DD composite laminate, therefore the objective of this work is to study the application to specimens representative of larger multi-stringer aeronautical structures. This paper focuses on the experimental investigation and numerical simulations of six SSCS manufactured using carbon NCFs and DD stacking sequence. Two control specimens have constant cross-sections, two are tapered, and two are tapered with a Teflon insert in the stiffener flange. After manufacturing, these specimens are tested by applying compression loads, inducing buckling, and ultimately failure. Numerical simulations are carried out, and specific features in the failure mechanism are discussed. In Section 2 and 3, the materials used in manufacturing and the specimens preparation procedure are presented, and the numerical models constructed for finite element analyses are described, respectively. In Section 4, the experimental setup and procedure are presented, followed by a discussion of both experimental and simulations results in Section 5. Finally, the paper concludes in Section 6.

2. Double-Double specimens manufacturing

The material used in the experiments is Chomarat's carbon NCF C-PLY™ T700. Two fabric types are utilized: one NCF features +45° and −45° orientations (hereon referred to as BX45), and the other with +30° and −30° orientations (BX30) [20,21]. These dry fabrics possess an areal-weight of 100 gsm (g/m^2) per bi-angle layer, or equivalently, approximately 50 g/m^2 per single ply. The dry fabrics are infused with epoxy resin via vacuum infusion and subsequently consolidated in an oven. A low-viscosity epoxy resin/hardener matrix system (ProSet INF 114/212) [22] is used in this out-of-autoclave (OoA) manufacturing process.

Separate manufacturing processes are employed for the skin and the omega hat stringer, which constitute the single-stringer specimens. Six specimens are manufactured at the University of Southern California for this series of tests: two as control specimens with constant thickness (Control1 and Control2 specimens), two tapered specimens (Taper1 and Taper2 specimens), and two tapered specimens featuring a Teflon insert being 40 mm long and 25 mm wide, i.e., the flange width, located at the center (in x-y plane) and mid-plane (z direction) of one of the stringer flanges (namely, Teflon1 and Teflon2 specimens). Despite their differences, all specimens maintain similar weight. A model of a single stringer specimen is presented in Fig. 1, where the main dimensions, as well as the position of the Teflon insert, are reported.

The control hats consist of 4 layers of 3 NCF C-PLY, where layers 1 and 3 utilize BX45 fabrics and layers 2 and 4 use BX30 fabrics. The layers are stacked according to the reference system in Fig. 1 along "z" direction. Similarly, the control skins comprise 2 layers of 5 NCF C-PLY, with layers 1 and 2 employing BX45 and BX30 fabrics, respectively. The stacking sequence can be defined as $[\pm 45_3/\pm 30_3/\pm 45_3/\pm 30_3]$ and $[\pm 45_5/\pm 30_5]$ for the hat and the skin, respectively. For the tapered hats, each of the 4 layers contains 6 plies: layers 1 and 3 feature BX45 fabrics, whereas layers 2 and 4 utilize BX30 fabrics. The taper width is 12.7 mm with a 6:1 tapered ratio per layer. Both the control and the tapered panels (skins) share a similar design composed of two layers, while the tapered panels have a 5:3 tapered ratio and the taper width is the same as for the hats. For the tapered specimens (Taper and Teflon), the stacking sequence can be defined as $[\pm 45_n/\pm 30_n/\pm 45_n/\pm 30_n]$ and $[\pm 45_n/\pm 30_n]$ for the hat and the skin, respectively; where "n" ranges from 1 to 6 and from 3 to 5 for the hat and the skin, respectively. Manufacturing these tapered specimens leverages a card-sliding technique [16], which offsets the layers according to the tapering strategy. By adopting this technique and DD stacking sequence, the design capability of composite structures are greatly enhanced, since the stacking sequence is kept consistent in the skin and the stringer, and the plies can be placed where the stiffness is mostly needed, i.e., in the stiffener cap, to maximize stiffness in the case of hat stiffener, at the same time reducing the plies in the flanges to have stronger and more flexible bonding. It is worth pointing out that the tapered specimens

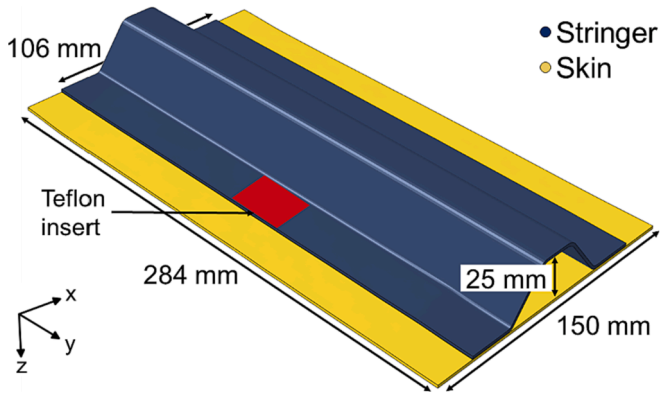

Fig. 1. A Single-Stringer Compression Specimen (SSCS).

utilize a non-symmetric balanced stacking sequence, which allows to aggressively taper the hat without abrupt thickness changes. Fig. 2 illustrates the schematic representations of the stacking sequence of the control (a), tapered (b), and Teflon (c) specimens, where each red bar indicates a NCF. The tapering technique, i.e., card-sliding, can be observed in Fig. 2(b) and Fig. 2(c), as well as the taper width highlighted in Fig. 2(b), and the position of the Teflon insert in Fig. 2(c).

Once the panels and hats are completed, they are sent to Delft University of Technology, where they are secondary bonded using the Scotchweld 9323 epoxy adhesive as per the manufacturer's specification [23]. The average adhesive thickness is 0.18 mm, measured using a digital caliper on the flanges of the control panels and verified post-test with an optical microscope through a cross-section cut of a specimen. Then, two potting tabs are molded at each end of the specimens using RenCast 2418-1 casting resin and Ren HY 5160 reacting agent to facilitate load introduced during the test [24]. After curing the casting resin as per manufacturer's specification, CNC (computer numerical control) machining ensures flat and parallel surfaces on the top and bottom of the specimens for optimal contact with the machine loading plates. The average thickness of the tabs after machining is 27.6 mm, and all measures are similar to the average, except for Control2 and Taper2 top tabs that are approximately 15 % lower.

In Table 1 average measures of the specimens are reported. For the control specimens, one average value of thickness is reported for the skins and hats. For the tapered specimens, several measurements were taken for the skins and the hats to capture the difference in the thickness, according to the tapering strategy reported in Fig. 2; in the Table 1 the average value of the measurements, the minimum and the maximum values are reported for the sake of conciseness. Also, it is worth underlining that the weight of the hats and skins was measured before beginning the bonding process.

The final step involves manually spraying a speckle pattern on the specimens for digital image correlation (DIC) utilization during the tests. Fig. 3 displays two prepared specimens with (a) a cross-section cut of the control and tapered specimens, in (b) a photo of two prepared specimens.

3. Finite element analysis

Numerical simulations are conducted at Politecnico di Milano and at Delft University of Technology. They were used prior to the experimental testing aimed to predict the behavior and failure modes of the specimens. These simulations were subsequently refined following the experimental phase to elucidate the test results more comprehensively.

The finite element analyses (FEA) employed the ABAQUS 2021"Quasi-Static" Dynamic Implicit solver [25], and automatic time stepping is used. The modeling of both the panel and stringer are executed using 8-node quadrilateral continuum shells (SC8R), each possessing a characteristic size of 1 mm. In regions involving free edges, which are not subjected to damage, a coarser mesh size of 1.5 mm is adopted. A single element through the thickness is used to model both the skin and the hat, with the composite stacking sequence assigned via the ABAQUS "Composite Layup" tool. Each ply, i.e., each UD ply constituting the NCF, is specified in the layup and is provided with 3 integration points, leading to distinct stacking sequences based on the location within the models. The stacking sequences defined in the

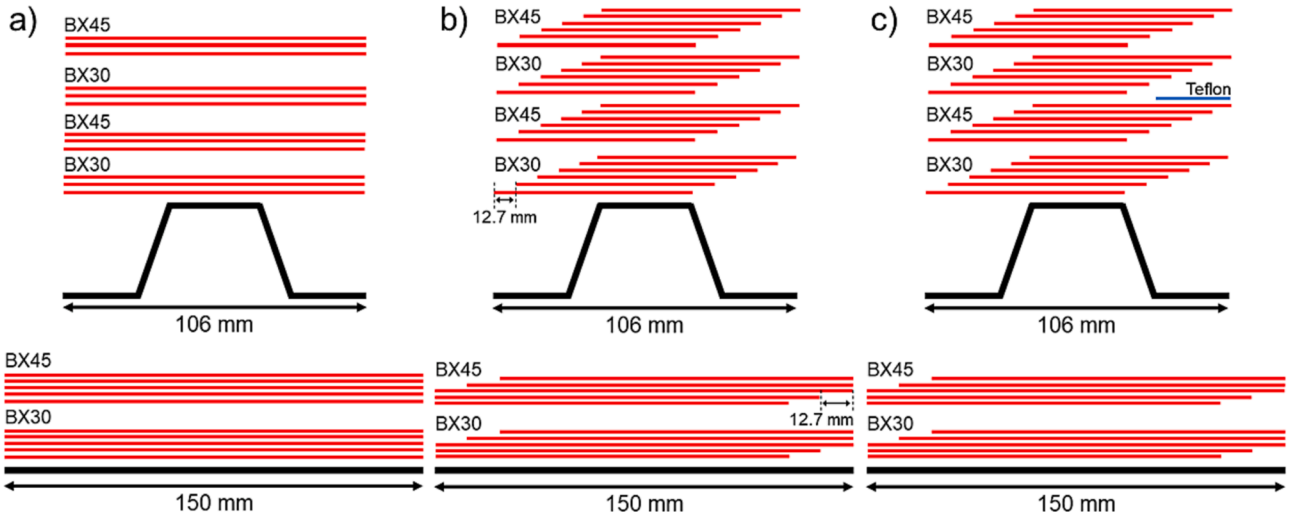

Fig. 2. Schematic Representation of the Stacking Sequence of the (a) Control, (b) Tapered and (c) Teflon specimens.

Table 1
Specimens Physical Properties.

	Control1	Control2	Taper1	Taper2	Teflon1	Teflon2
Skin Width [mm]	149.97	149.84	149.73	149.64	149.67	149.96
Hat Width [mm]	106.98	105.80	105.61	106.04	106.91	105.26
Hat Angle [°]	53	52	52	52	54	53
Hat Height [mm]	25.34	25.32	25.35	25.28	25.13	24.99
Specimen Length [mm]	284.95	283.99	284.91	284.35	285.27	282.94
Hat t_{avg} [mm]	1.57	1.54	1.72	1.70	1.76	1.85
Skin t_{avg} [mm]	1.67	1.95	1.48	1.30	1.32	1.97
Hat t_{min}	–	–	0.76	0.77	0.79	0.74
Hat t_{max}	–	–	2.75	2.68	2.80	3.04
Skin t_{min}	–	–	1.24	1.11	1.09	1.71
Skin t_{max}	–	–	1.65	1.43	1.51	2.14
Skin Weight [g]	92.9	106.3	86.1	76.1	78.5	110.1
Hat Weight [g]	80.8	77	80.5	81.9	87.2	89.8

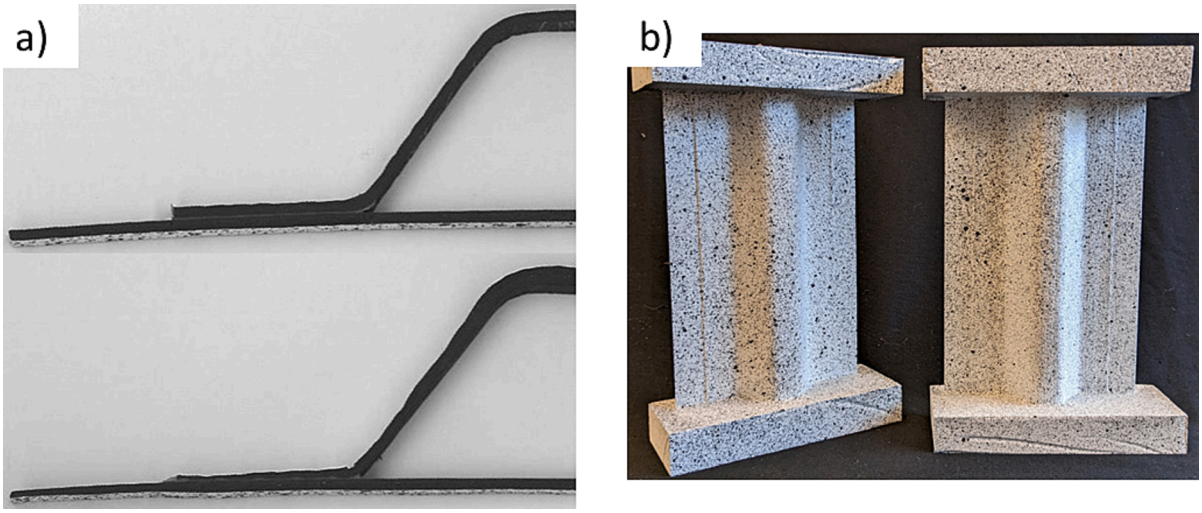

Fig. 3. (a) Cross-Section Cut of the Control (top) and Tapered (bottom) Specimens, (b) two Single Stringer Specimens.

ABAQUS "Composite Layup" tool are the same as those specified earlier in Section 2. Fig. 4 presents a symmetric cross-section of the Taper1 FE model, illustrating each section with different colors, corresponding to the varied stacking sequence. From Fig. 4 it can be noted that in the FEM model the ply-drops resulting from the tapering of the section are not modelled, and the thickness is varied continuously from the thinnest point in the flange, to the thickest at the top of the stringer (same method is applied to the skin); this decision was supported by a visual inspection of the specimens, as the ply-drops are barely visible and thickness changes are small. To ease the connection of the skin and the stringer, the layer of cohesive elements lies on the flat surfaces of the skin and the stringer, whose tapering then occurs on the opposite side.

The hat with Teflon insert in the flange is modelled with two elements through its thickness, effectively bisecting the hat along its mid-plane. A frictionless hard-contact interaction is attributed to the Teflon-insert area, while a cohesive zone model governs contact interactions 30 mm proximal and distal to the insert, accounting for potential crack propagation from the insert position. The intra-laminar damage within the composites is accounted for via ABAQUS' built-in Hashin failure criteria [26], with progressive damage managed through a linear softening law. The adhesive interaction is represented by three-dimensional cohesive elements (COH3D8), governed by the cohesive zone model and the Benzeggagh-Kenane fracture criterion with linear degradation of cohesive elements properties [27]. These cohesive elements, along with their surrounding elements, possess a characteristic size of 0.25 mm. This sizing ensures a minimum of three cohesive elements within the cohesive processing zone [28].

Boundary conditions of the FE model allow constrained displacement in sections corresponding to the potting but permit freedom along the longitudinal axis. At the specimen ends, one edge is fixed, while the other is limited in all degrees of freedom except the one applied to end shortening [29].

Incorporation of geometrical imperfections is a necessity in the FE model given the high sensitivity of buckling behavior in thin-walled structures to such imperfections. Residual stresses from manufacturing, however, are overlooked. Out of plane displacements are applied to the back of the skin to introduce geometrical imperfections, using interpolated data from the initial DIC acquisition of the position of the panel. A preliminary FE linear analysis is conducted with a nominal mesh density, and the resulting node-file is employed for non-linear analysis, transferring only the deformation field [30].

Material properties are sourced from existing literatures and reported in Table 2 for the composite skin and stringers, and for the adhesive material in Table 3.

Specifically, for the NCF intra-laminar properties, the work of Arteiro et al. where a similar type of fabric from the same manufacturer was examined [18], while fracture toughness properties are adopted from Camanho et al. [31]. The cohesive zone properties for the Scotchweld 9323 are adopted from Santaniello et al. [32]. However, in order to align the model with the specimen weight (as reported in Table 1), a lower fiber volume content is assumed, i.e., 35 % w/w, resulting in 1.35 g/cm^3 density. Then the longitudinal modulus and the fibers mode strength are scaled according to the new fiber volume content. The longitudinal modulus is the only engineering constant decreased because it is the main contributor to the specimen stiffness; the fibers mode strength values are reduced for consistency, even though they are less relevant

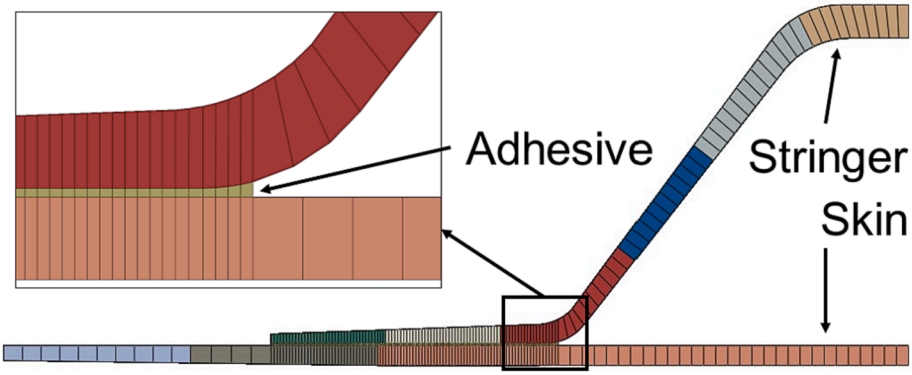

Fig. 4. Cross-Sectional View of a Taper1 Single-Stringer Specimen Model.

Table 2
Engineering Properties, Ply Strength and Fracture Toughness of the Carbon Composite Material [18,31].

Property	Unit	Value
E_1	[GPa]	110
E_2	[GPa]	7.4
ν_{12}	[ ]	0.30
G_{12}	[GPa]	4.2
X_T	[MPa]	2300
X_C	[MPa]	1500
Y_T	[MPa]	66
Y_C	[MPa]	220
S_L	[MPa]	93
GF(+)	[N/mm]	81.5
GF(-)	[N/mm]	106.3
GMI	[N/mm]	0.277
GMII	[N/mm]	0.788

Table 3
Adhesive Cohesive Zone Properties [32].

Property	Unit	Value
E_{nn}	[MPa]	2110
E_{ss}	[MPa]	460.5
t_n	[MPa]	21.9
t_s	[MPa]	24.2
G_n^c	[N/mm]	0.449
G_s^c	[N/mm]	7.53
η	[ ]	1.53

since failure tends to be triggered by skin-stringer separation. In addition, a critical observation was that the experimentally determined failure load was lower than that predicted in preliminary analysis, suggesting an overestimation of adhesive toughness in [32]. For instance, the FEM simulation of Control1 specimen carried out with nominal properties, resulted in a maximum force of 93.2 kN (and a stiffness of 55.1 kN/mm); which is higher than the result presented in Subsection 5.1. Hence, the mode I and mode II/III fracture toughness of the adhesive in the present models are considered to be the same as in [31]. These hypotheses are deemed acceptable given the primary objective of this study, which is to investigate the behavior and the failure mode of specimens manufactured with the DD stacking sequence.

4. Experimental setup

To investigate buckling, post-buckling behavior, and the ultimate failure mode, single stringer specimens are tested at Delft University of Technology using an MTS machine capable of exerting 250 kN under compression. The experimental setup is demonstrated in Fig. 5. The specimen is positioned between two plates, the top one remaining stationary while the bottom applies the compression load. Employed to monitor vertical displacement and ensure evenly distributed loads are two Linear Displacement Sensors (LDS) targeting the compression plates. Two DIC systems using 5 MP cameras capture displacement in all three directions at the front and back of the specimens. The acquisition frequency for the load cell, the compression plate displacement and the two lasers is 100 Hz; while the two DIC systems acquisition frequency is 1/3 Hz, synchronized with the other instruments.

For each specimen, a series of 3 to 4 preliminary stiffness tests is performed, each applying a load up to 25 kN, before increasing the load further. These tests ensure the consistency of stiffness across different trails, and accommodate any possible tab settling. Following these initial stiffness tests, the same specimen is subjected to further loads without any adjustments to the specimen position, or the machine settings. Specimens labelled Control1, Taper1 and Teflon1 are tested to the point of failure, as they exhibit the most consistent and comparable thickness among the group. Conversely, specimens Control2, Taper2, and Teflon2 are tested progressively increasing the load in 5 kN increments, until visible damage or a noticeable sound is detected. In such cases, the test is halted, and an ultrasound inspection is conducted. The procedure continues in iterations until the specimen ultimately fails.

5. Results and discussion

5.1. Experimental and numerical load-displacement curves

Fig. 6 presents the experimental load–displacement curves of the 6 tested specimens. The force is plotted as a function of the vertical displacement, measured by the DIC, and calculated as the difference between the top and bottom tabs. In Table 4 the experimental results are summarized, reporting the maximum force, the displacement at failure, and the stiffness, evaluated in the 20–10 kN linear interval of the force vs displacement curve. For the Control2 and Taper2 specimens, the curve of the last test run, that lead to the specimens failure, is plotted, because it was not possible to detect damage before the specimens collapsed. For the Teflon2 specimen, the curve of the penultimate test is plotted, because damage was detected with the C-Scan inspection for this specimen, and when the last test was run, the specimens collapsed at the same maximum load recorded in the previous one; this aspect will be further discussed in Subsection 5.3 where the failure mode of the specimens is addressed. It is noteworthy that the Control2 specimen failed near the tabs, which makes unreliable the comparison of the maximum force and displacement at failure with the other specimens.

Due to considerable variations in thickness after manufacturing, the failure loads also varied, even among the same type of specimens. Consequently, only Control1, Taper1, and Teflon1 specimens, due to

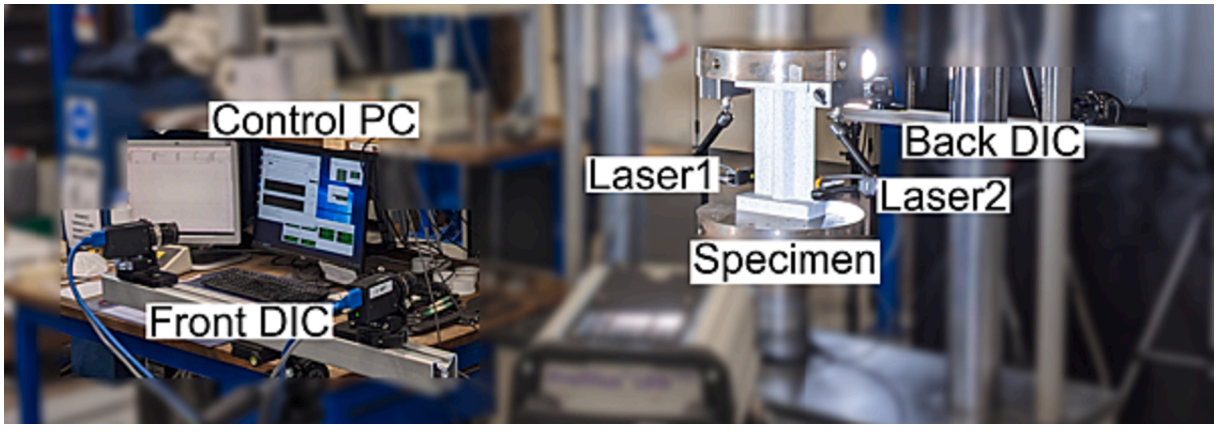

Fig. 5. Experimental Setup at Delft University of Technology.

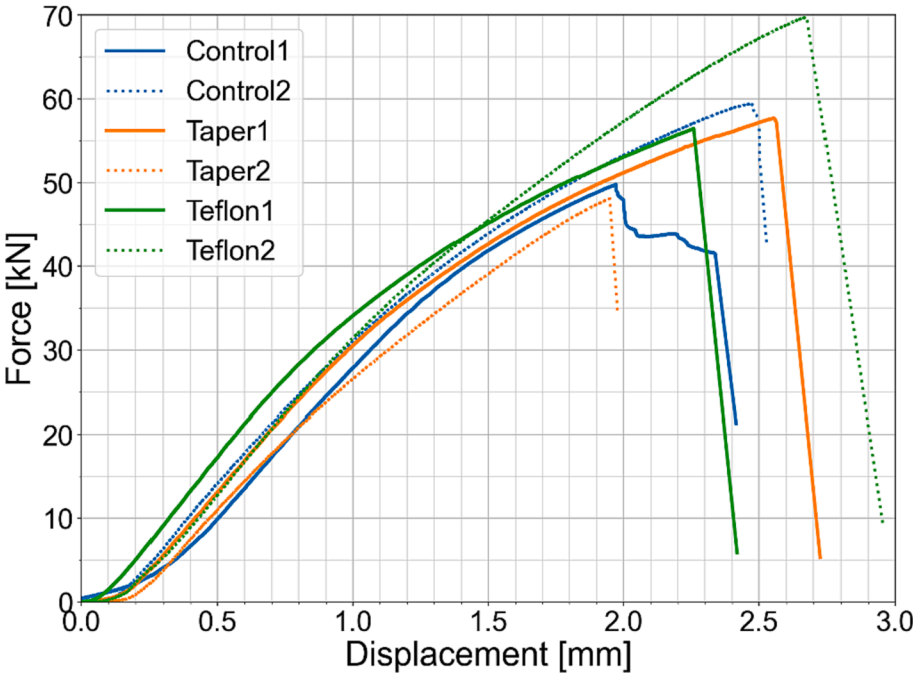

Fig. 6. Experimental Load vs. Displacement Curves.

Table 4
Summary of Experimental Results.

	Maximum Force [kN]	Displacement at Collapse [mm]	Stiffness [kN/mm]
Control1	49.8	2.33	40.3
Control2	59.4	2.46	39.5
Taper1	57.7	2.55	42.0
Taper2	48.1	1.94	34.8
Teflon1	56.5	2.25	42.2
Teflon2	69.7	2.67	40.2

their similar thickness and weight, were considered for comparison with the FEA results. Despite these variations, buckling shapes and failure modes remain consistent within the same group of specimens, as will be discussed later in this Section. This consistency supports the validity of comparing the three aforementioned specimens with FEA models. Fig. 7 compares the compression force versus displacement curves of these three experimental specimens with FEA results. Table 5 reports the maximum force, displacement at failure, stiffness, and the percentage error. The percentage error is evaluated as the difference between FEA and experimental results, normalized by the experimental value. All experimental curves are plotted with a displacement offset for accuracy,

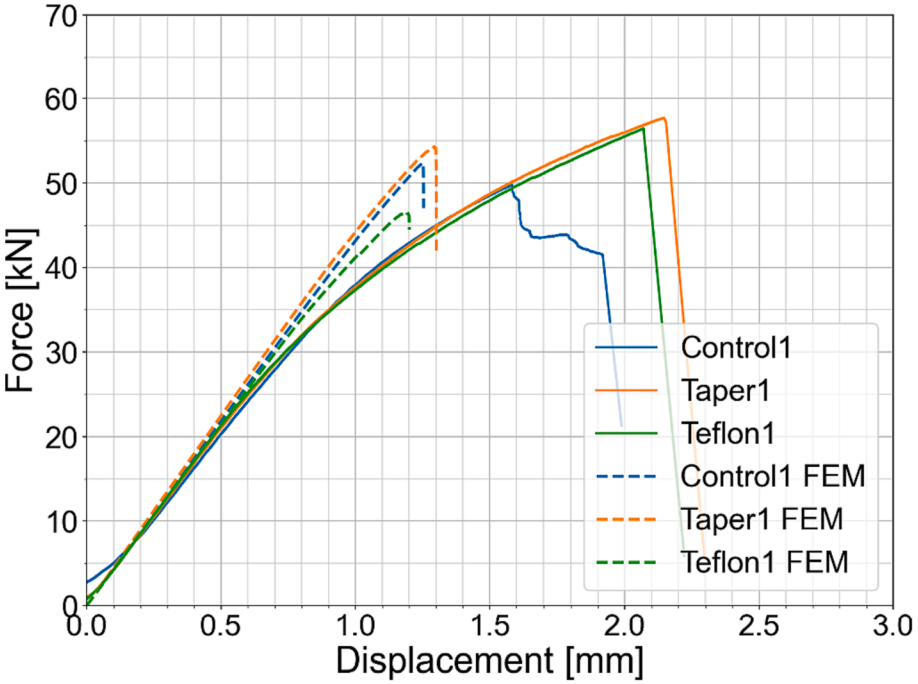

Fig. 7. Numerical vs. Experimental Load-Displacement Curves.

Table 5
Summary of Numerical and Experimental Results.

	Maximum Force	Displacement at Collapse	Stiffness
Control1	49.8 kN	1.92 mm	40.3 kN/mm
Control1 FEM	52.4 kN	1.25 mm	43.6 kN/mm
|Percentage Error|	5.2 %	34.9 %	8.2 %
Taper1	57.7 kN	2.14 mm	42.0 kN/mm
Taper1 FEM	54.3 kN	1.29 mm	44.9 kN/mm
|Percentage Error|	5.9 %	39.7 %	6.9 %
Teflon1	56.5 kN	2.07 mm	42.2 kN/mm
Teflon1 FEM	46.6 kN	1.19 mm	41.5 kN/mm
|Percentage Error|	17.5 %	42.5 %	1.7 %

ignoring the initial compliance of the specimens related mainly to the potted tabs, and the values reported in Table 5 are updated, accounting for the offset.

The FEA simulations accurately predicted the stiffness, and the maximum forces are comparable with the experimental values. However, the FEA models show a predominantly linear curve until reaching maximum force, contrasting the strong non-linear behavior displayed by experimental specimens around 30 kN. This non-linearity led to differences in the displacement at failure, which might be attributed to the assumptions and inherent approximations of the FEM model. For instance, the FEA model neglected the compliance of the potting material in boundary conditions, and the built-in material model used in ABAQUS demonstrated a linear shear behavior. Such approximations can affect specimen stiffness, especially given the stacking sequence investigated in this work that lacks plies oriented along the longitudinal direction.

5.2. Out-of-plane displacement

The out-of-plane displacement recorded using the two DIC systems, showed consistent behavior among the specimens. The tapered specimens, with and without Teflon inserts, demonstrated virtually identical displacement contours. Fig. 8 shows four contour plots for the Taper1 specimen to illustrate the evolution of the post-buckling deformation. An animated gif is also provided as supplementary content, showing the evolution of the experimental out of plane displacement recorded by the back DIC system.

Outward displacement from the stringer to the camera viewpoint is indicated with positive signs, while inward direction towards the stringer is marked as negative. In comparing contour plots with numerical results, both Taper and Teflon specimens initially exhibit one half-wave at the free edges of the skin, which then transitions into three waves at approximately 30 kN. Fig. 8 illustrates that the out-of-plane displacement progressively amplifies with the load until skin-stringer separation triggers failure, originating under the hat flanges due to mode-I opening. Despite the identical buckling shape, the FEA model underestimates the out-of-plane displacement, a discrepancy stemming from the smaller end shortening of the model at the same compression load.

Fig. 9(a) and Fig. 9(b) respectively demonstrated the out-of-plane displacement of Control1 and Teflon1 specimens at their maximum force. Unlike the tapered specimens, the Control1 specimen portrays a unique behavior, presenting three half waves under the hat while the skin buckles with only one half wave at the free edges. The contour at maximum force in the FEM analysis of the Control1 specimen differs slightly, as it displays one half wave at one free edges, and three at the other, akin to the tapered panels. This variation may be attributed to geometrical imperfections and inaccuracies in boundary conditions.

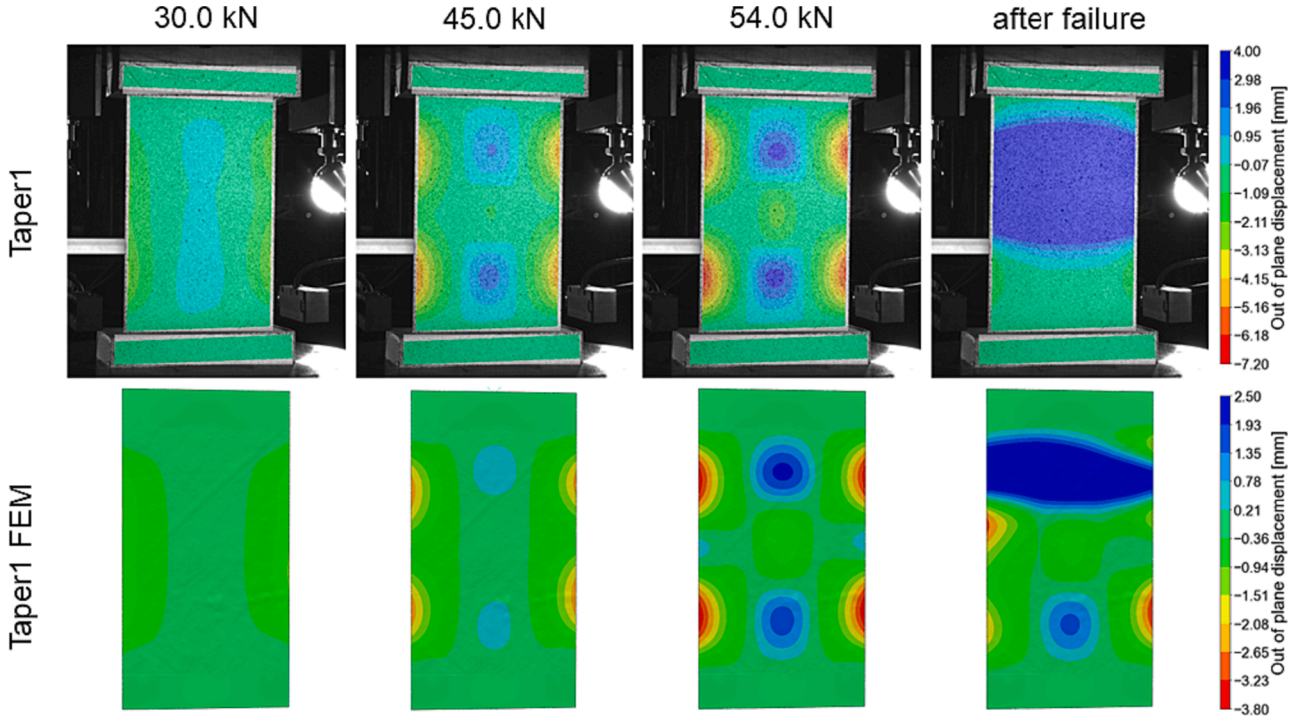

Fig. 8. Numerical and Experimental Comparison of the Taper1 Specimen's Out-of-Plane Displacement under increasing Compression Force.

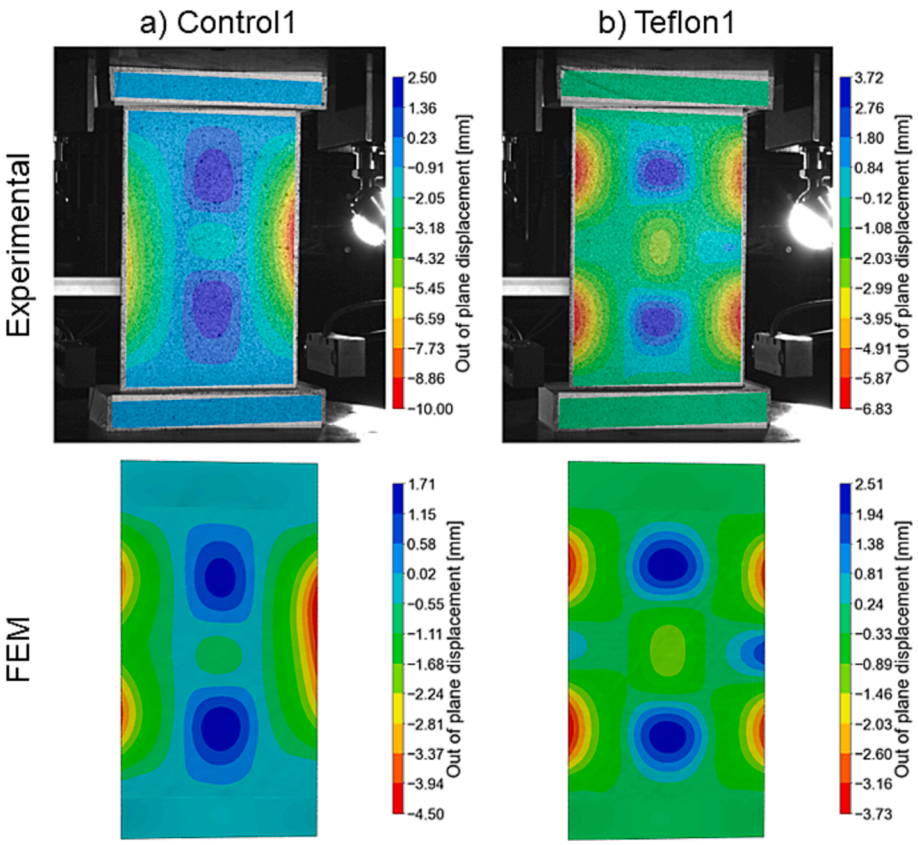

Fig. 9. Numerical and Experimental Comparison of (a) Control1, and (b) Teflon1 Specimens' Out-of-Plane Displacement at Maximum Force.

Observing that Taper and Teflon specimens exhibit similar buckling shapes, the out-of-plane displacement contour for Teflon1 in Fig. 9(b) closely mirrors Fig. 8′s depiction of the Taper1 specimen, with three half waves characterizing the post-buckling shape. It is noteworthy that the Teflon insert influences the shape, resulting in a larger outward out-of-plane displacement on the insert side (right) compared to the other free edge. This disparity is more pronounced in the FEA analysis.

Fig. 10(a) presents the contour plot of Control1 specimen post-maximum force, revealing skin-stringer separation (at the top left corner of the specimen) beyond the peak load, although the structure continues bearing load until collapse. In the experimental test, the portion of the curve between the maximum load and the collapse is marked by an almost constant load despite increasing compression displacement. This behavior is mirrored in the numerical analysis, although the point of collapse in the FEM analysis coincides with the maximum force. Only the Control1 specimen exhibits this behavior, suggesting a potential defect, possibly in the bonding line. Fig. 10(b) offers a frontal view of the out-of-plane displacement of the Teflon1 specimen at maximum force. Close to the maximum force, the flange section housing the insert buckles locally, effectively separating from the rest of the flange. This phenomenon, captured both in DIC images and FEM simulations, exhibits local inward displacement towards the stringer at the insert location. The delamination does not further propagate through the flange thickness, suggesting good toughness for the composite laminate. All specimens ultimately fail due to mode-I opening.

In Fig. 11 the out-of-plane displacement contour plots of the Control2, Taper2, and Teflon2 specimens is shown. The FE simulations of these specimens were not carried out, as explained in the previous Subsection. The behavior of the Control2 specimen in Fig. 11(a) is identical to that of Control1 specimen, however, it can be noted that the positive displacement close to the top tab differs from the half-wave close to the bottom and from the contour plots previously shown in this Subsection; this likely explains the unusual failure occurred to this specimen. The reason for this anomaly is probably explained by issues in the boundary condition of the specimen, e.g., the top tab being too thin. Regarding the Taper2 and Teflon2 specimens, the behavior is consistent with the others.

The experimental outward (+) maximum out-of-plane displacement is similar for the Taper2, Teflon1 and Teflon2 specimens, but it is significantly lower for Control1, Control2 and Taper1 specimens, that showed unexpected failure modes or failed at lower compression displacement. The experimental inward (-) maximum out-of-plane displacement is generally larger than the outward (+) displacement, and similar discrepancies are found among the specimens as those observed for the outward (+) displacement. The results from the FEM simulations are lower than the experimental results, suggesting that the assumption made for the adhesive toughness was excessively conservative.

5.3. Failure mode

Fig. 12 exhibits the photographs captured after the Control1, Taper1 and Teflon1 specimens collapsed. The damage mechanisms are consistent across all specimens, except for Control2 specimen for which failure occurred near the tab. Evidenced by DIC data, the specimen collapse is caused by the skin-stringer separation due to mode-I opening nucleating in the flange under the hat and progressing outward towards the free edge. The half waves displacing outwards from the stringer, those generating the stress leading to failure in the adhesive joint, are located near the tabs, causing separation away from the specimen center. Skin-stringer separation is highlighted with red arrows in the Fig. 12, and it is clearly visible in the specimens. The tests revealed fibers pullout near the skin and stringer separation zone, indicated by orange arrows. This skin-stringer separation impairs the load-bearing capability of the structure, thereby inciting the crippling of the stringer, as visibly

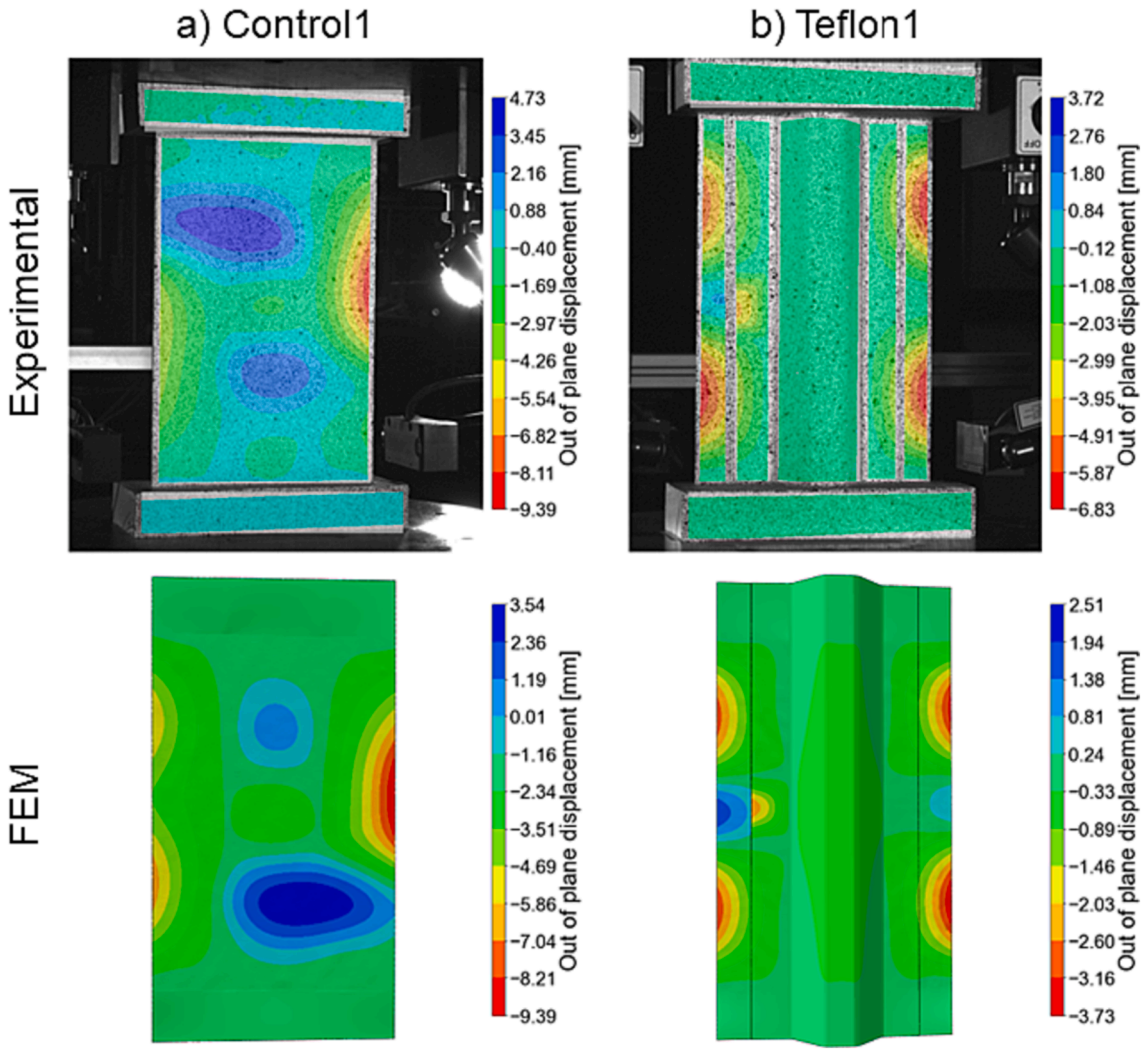

Fig. 10. (a) Out-of-Plane Displacement of Control1 Specimen Post-Maximum Force, and (b) front view of Teflon1 Specimen at Maximum Force.

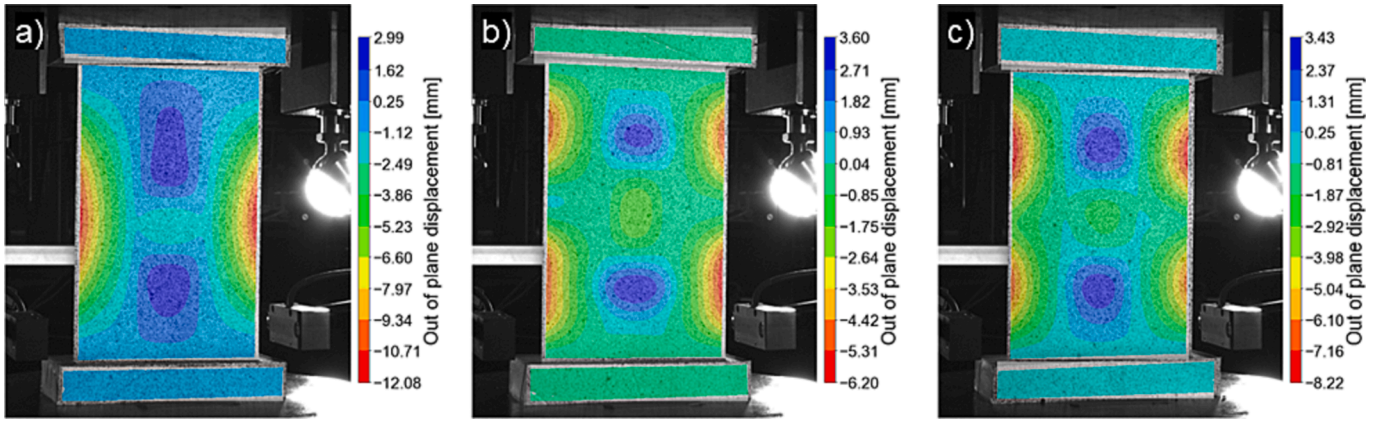

Fig. 11. (a) Control2, (b) Taper2, and (c) Teflon2 Specimens Out-of-Plane Displacement at Maximum Force.

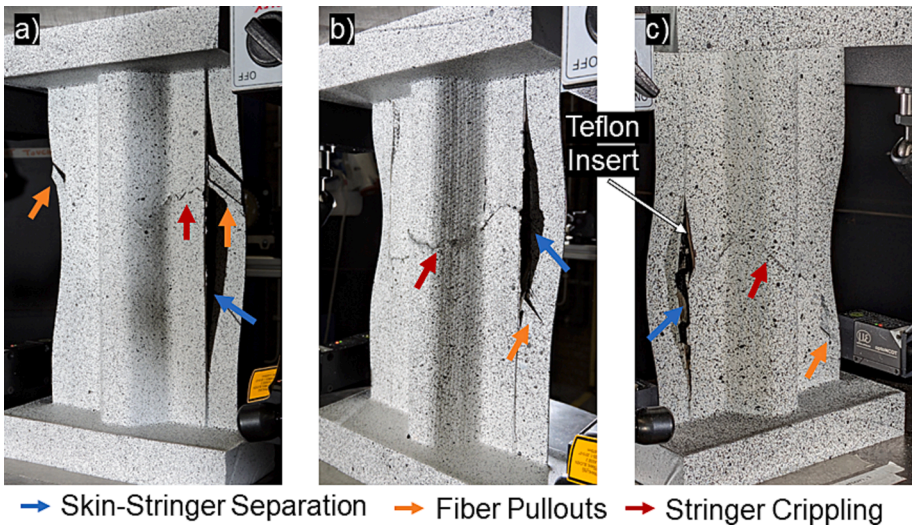

Fig. 12. Failure Modes of the of (a) Control1, (b) Taper1 and (c) Teflon1 Specimens.

highlighted in the images. In the pictures of Taper1 and Teflon1 specimens, the blue arrows indicate the crack running through the entire stringer section of the hat. For the Control1 specimen, one crack initiates lower in the flange and proceeds to the top of the hat; this variance is presumably connected to the differing maximum loads the specimens endured, with the Control1 enduring a lower maximum load (approximately 15 %, compared to Taper1 and Teflon1 specimens). The crack follows an irregular trajectory; in the flanges of the Taper1 specimen, the direction of the crack is orthogonal to the longitudinal direction of the specimen, yet on closer inspection, it locally aligns with the fibers direction, which are not oriented along the longitudinal direction. The cracks tend to alter direction on the webs of the hat, exhibiting a fracture roughly oriented at 45°, and then globally orthogonal to the stringer direction at the top flange of the hat. In the Fig. 12 the Teflon insert is visible and indicated by a white arrow, the local buckling of the flange inward towards the hat, where the Teflon insert resides, can be noted, as highlighted in the preceding Subsection. An animated gif is provided as supplementary content, showing the video of the failure of Taper1 specimen observed from the front, recorded by a photo camera.

The comparison of the results in Fig. 12 with FEM models is not provided. Skin-stringer separation is driven by cohesive elements failure, and it will be discussed in detail in the next Subsection, highlighting specific features related to the geometries of the investigated specimens. Stringer crippling is related to the failure of the composite laminae (intra-laminar damage), which occurs after the skin and the stringer separate, and the force drops. This implies that stringer crippling does not contribute to collapse, rather it results from the collapse. Simulating this phenomenon with FE simulations is computationally expensive, because the time step increment is small when several elements (the cohesive elements modelling the adhesive) have failed; hence it was decided to stop the simulation shortly after the maximum load was reached, because it would not contribute to explain the damage mechanisms leading to collapse. Regarding fibers pullout, the phenomenon is unfeasible to be modelled with FEM models and requires a different level of details, that is beyond the scope of this work.

Fig. 13 illustrates the fracture surface of the Control1 specimen, attained by the tabs and forcing the complete separation of the hat and stringer post-test. The two highlighted red circles indicate the failed bonding parts in the flange leading to the collapse of the single stringer specimen. Particularly, the right circle corresponds to the first part that failed (see Fig. 10(a)). The fracture surface examination reveals adhesive failure, indicating suboptimal adhesion between the adhesive and composites. This could result from multiple factors involved in the adhesive joint preparation process, and likely underlies the unique force

Fig. 13. Control1 Specimen Fracture Surface.

vs. displacement curve exhibited by the Control1 specimen. Pre-testing C-Scan inspection, however, showed no abnormalities in any specimens. Fig. 14 presents the C-Scan inspection performed at 65 kN (left) and 70

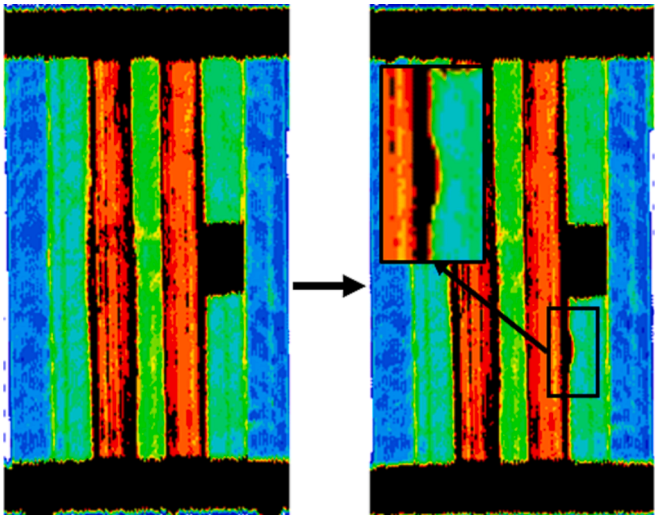

Fig. 14. C-Scan showing the Initiation of Skin-Stringer Separation in Teflon2 Specimen.

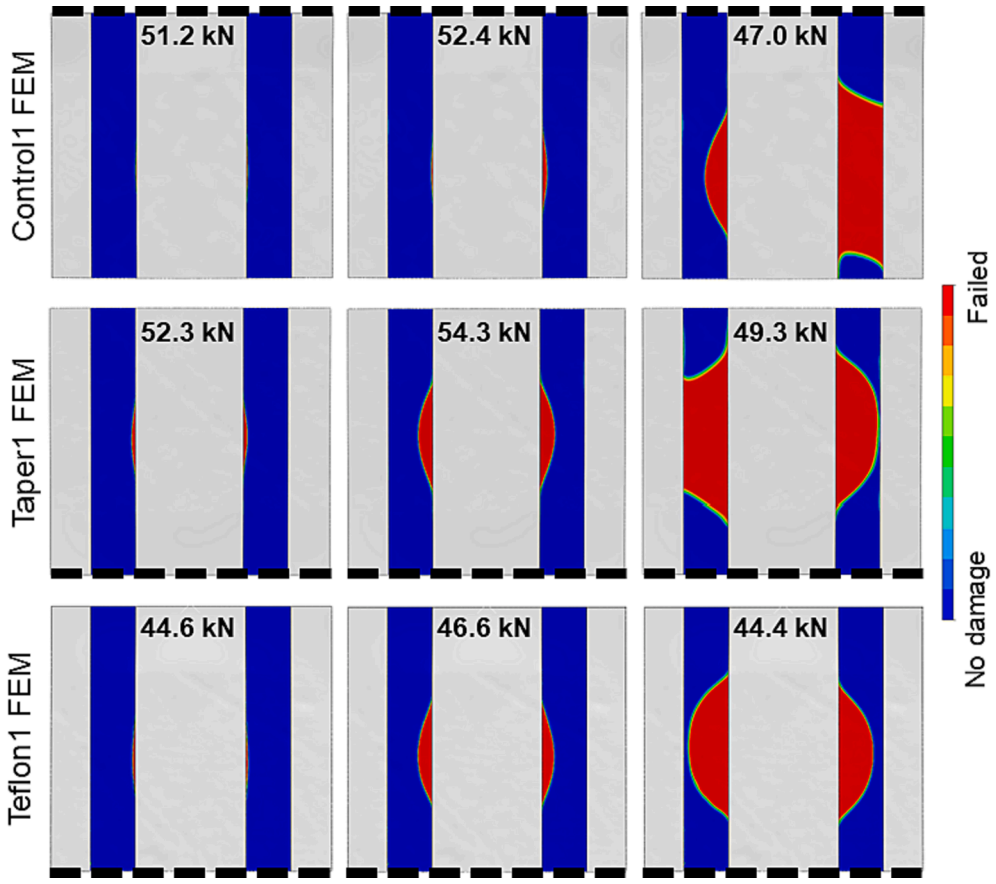

Fig. 15. Cohesive Elements Damage Variable Contour Plots.

kN (right) on the Teflon2 specimen. After the latter inspection, the final test was run, causing the specimen to fail at nearly the same load. The image clearly shows delamination initiation at the bottom right where the black square is magnified. The snapshot provides robust support for the failure mode described and unequivocally shows that the separation initiated at this point, leading to crippling, as no other damage was detectable with C-Scan or visual inspections. The same procedure performed on Control2 and Taper1 did not reveal the onset of the damage.

5.4. *Tapering effect*

The preceding subsections underlined that skin-stringer separation is the main catalyst for specimen failure, resulting in subsequent stringer crippling. This phenomenon is aptly represented by the FE models, offering insights into the impact of the two distinct geometries proposed in this study. Fig. 15 features three images for each FE model, depicting the progression of the cohesive element damage variable at different stages of the force vs. displacement curve: before (left), at (middle), and after (right) the maximum load. Only one half of the model, where separation took place, is shown, and the dashed lines indicate the cutting plane location. Based on the FE models, tapering influences failure, enabling the tapered specimens to endure more extensive damage before collapsing. For instance, examining the damage area evolution in the Control1 FE model reveals a minor red area at maximum load and negligible failed cohesive elements before the maximum load. Additionally, it is noteworthy that the separation in the two tapered specimens progresses almost uniformly in the two flanges, whereas in the control specimen the flange on one side has entirely failed at 47 kN, and a significant number of elements on the other side have not yet failed.

As expected, the pictures presented in the middle column in Fig. 15 closely resemble the shape of the delaminated area in the flange captured in Fig. 14, shown in the previous Subsection; also, the location of the failed cohesive elements matches well the experimental evidence, i.e., nucleating in the flange under the hat near the half wave displacing outwards from the stringer.

Fig. 16 presents the mode mix ratios at the damage initiation (MMIXDMI) and the damage evolution (MMIXDME) in the cohesive elements. A ratio equal to 0, i.e., blue color in the contour plot, denotes a failure dominated by mode-I opening, while a ratio of 1, i.e., in red color, suggests mode II/III dominated failure. The ABAQUS variable shown in the plots does not distinguish between mode II and mode III. Observations reveal that damage initiation is primarily driven by mode I, but it transitions to mode II/III as separation advances through the flange width and along the specimen length. This suggests that the Control1 specimen dissipates most of its fracture energy through a mode I failure, while the tapered specimens employ both damage mechanisms and, more importantly, can dissipate more energy, less abruptly, before collapsing. The images, particularly for the Taper1 FEM simulation, suggest that flange tapering fosters the transition from a Mode I mechanism to mode II/III, which are inherently tougher failure mechanisms. These last observations suggest that adopting DD stacking sequence, and exploiting the card sliding manufacturing technique, can result in enhanced structural performance of composite structures.

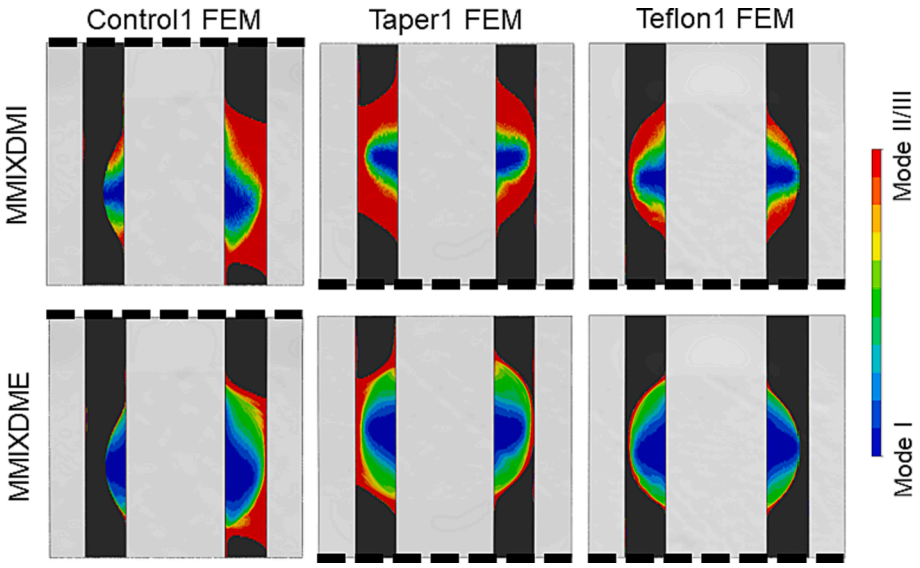

Fig. 16. Mode Mixity of Cohesive Elements for Damage Initiation (MMIXDMI), and Damage Evolution (MMIXDME).

6. Conclusion

This study involved the manufacturing and testing of six DD single stringer specimens, to investigate the post-buckling behavior and collapse under compression loading conditions. These specimens were composed of repeating [±45] and [±30] NCFs, resulting in a Double-Double stacking sequence. Utilizing the card-sliding technique, the specimens were manufactured with an offset to achieve a tapered cross-section. Two specimens with a constant cross section were produced, along with four with a tapered cross-section, two of which contained a Teflon insert in the stringer flange. The specimens were prepared for testing, and compression load was applied to scrutinize their buckling, post-buckling, and failure behavior. The study employed numerical simulations validated by the experimental tests to compare the experimental observations and investigate damage mechanism and collapse. While the force vs. displacement curves demonstrated similar stiffness and maximum compression load, the FEM curves were predominantly linear, unlike the experimental curves, which were non-linear post-30 kN. This discrepancy likely underscores the limitations of the employed material model, which does not account for shear non-linearity, and emphasizes the significance of coupon-level characterization before progressing to larger sub-structures. The specimens exhibited a post-buckling shape with three half waves under the hat and at the free edges, except for the experimental control panels, which showed only one half wave in their free edges. Failure was primarily attributed to skin-stringer separation, leading to specimens collapse and subsequent stringer crippling. The Teflon insert placed in the middle of the hat flange section negligibly affected the failure mode and failure load. A section of the results was dedicated to emphasizing the effect of severe hats tapering, a notable feature achievable with DD and card-sliding technique. FEM simulations underscored that tapering modifies the damage area, resulting in a structure capable of enduring a larger extent of damage before collapsing. It is critical to note that the full benefits of tapered flanges can be realized by designing delamination to initiate outside, rather than under, the hat.

This work showed the possible advantages, which warrant further investigation, of adopting a DD stacking sequence. It suggests the possibility of designing composite structures less susceptible to delamination, implying that exploring co-cured structures could pave the way for wider applications. This could potentially decrease the susceptibility of composite to delamination and promote intra-laminar failure.

CRediT authorship contribution statement

A. Vescovini: Conceptualization, Methodology, Investigation, Validation, Writing – original draft. **C.X. Li:** Conceptualization, Methodology, Investigation, Writing – review & editing. **J. Paz:** Methodology, Investigation, Writing – review & editing. **B. Jin:** Conceptualization, Methodology, Writing – review & editing, Supervision, Funding acquisition. **A. Manes:** Conceptualization, Writing – review & editing, Supervision. **C. Bisagni:** Conceptualization, Methodology, Investigation, Writing – review & editing, Supervision, Funding acquisition.

Declaration of competing interest

The authors declare that they have no known competing financial interests or personal relationships that could have appeared to influence the work reported in this paper.

Data availability

Data will be made available on request.

Acknowledgements

The authors would like to thank Prof. S.W. Tsai (Stanford University, USA) for the useful discussions and Dr. Erik Kappel of the German Aerospace Center (DLR) for the support in the design of the specimens.

Appendix A. Supplementary material

Supplementary data to this article can be found online at https://doi.org/10.1016/j.compstruct.2023.117699.

References

[1] Falzon BG, Stevens KA, Davies GO. Postbucking behaviour of a blade-stiffened composite panel loaded in uniaxial compression. Compos Part A Appl Sci Manuf 2000;31:459–68. https://doi.org/10.1016/S1359-835X(99)00085-8.
[2] Zimmermann R, Klein H, Kling A. Buckling and postbuckling of stringer stiffened fibre composite curved panels - Tests and computations. Compos Struct 2006;73:150–61. https://doi.org/10.1016/J.COMPSTRUCT.2005.11.050.
[3] Degenhardt R, Kling A, Klein H, Hillger W, Goetting HC, Zimmermann R, et al. Experiments on buckling and postbuckling of thin-walled CFRP structures using advanced measurement systems. Int J Struct Stab Dyn 2007;7:337–58. https://doi.org/10.1142/S0219455407002253.

[4] Abramovich H, Weller T, Bisagni C. Buckling behavior of composite laminated stiffened panels under combined shear-axial compression. J Aircr 2008;45:402–13. https://doi.org/10.2514/1.27635.
[5] Abramovich H, Weller T. Repeated buckling and postbuckling behavior of laminated stringer-stiffened composite panels with and without damage. Int J Struct Stab Dyn 2010;10:807–25. https://doi.org/10.1142/S0219455410003750.
[6] Bisagni C, Vescovini R, Dávila CG. Single-stringer compression specimen for the assessment of damage tolerance of postbuckled structures. J Aircr 2011;48:495–502. https://doi.org/10.2514/1.C031106.
[7] Bisagni C, Dávila CG. Experimental investigation of the postbuckling response and collapse of a single-stringer specimen. Compos Struct 2014;108:493–503. https://doi.org/10.1016/j.compstruct.2013.09.018.
[8] Vescovini R, Dávila CG, Bisagni C. Failure analysis of composite multi-stringer panels using simplified models. Compos Part B Eng 2013;45:939–51. https://doi.org/10.1016/j.compositesb.2012.07.030.
[9] Dávila CG, Bisagni C. Fatigue life and damage tolerance of postbuckled composite stiffened structures with indentation damage. J Compos Mater 2018;52:931–43. https://doi.org/10.1177/0021998317715785.
[10] Kootte LJ, Bisagni C. A Methodology to Investigate Skin-Stringer Separation in Postbuckled Composite Stiffened Panels. AIAA SciTech 2020 forum, vol. 2020–0477, 2020. https://doi.org/https://doi.org/10.2514/6.2020-0477.
[11] Tsai SW, Sharma N, Arteiro A, Roy S, Rainsberger B. Composite Double-Double and Grid/Skin Structures - Low Weight/Low Cost Design and Manufacturing. Stanford, CA 94305-4035: Stanford University Composite Design Group; 2019.
[12] Tsai SW, Melo JDD. Composite Materials Design and Testing. Stanford, CA 94305-4035: Stanford University Composite Design Group; 2015.
[13] Shrivastava S, Sharma N, Tsai SW, Mohite PM. D and DD-drop layup optimization of aircraft wing panels under multi-load case design environment. Compos Struct 2020:248. https://doi.org/10.1016/J.COMPSTRUCT.2020.112518.
[14] Vermes B, Tsai SW, Massard T, Springer GS, Czigany T. Design of laminates by a novel "double–double" layup. Thin-Walled Struct 2021;165:107954. https://doi.org/10.1016/j.tws.2021.107954.
[15] Kappel E. Double-Double laminates for aerospace applications — Finding best laminates for given load sets. Compos Part C Open. Access 2022:8. https://doi.org/10.1016/J.JCOMC.2022.100244.
[16] Tsai SW. Double-Double: New Family of Composite Laminates. AIAA J 2021;59:4293–305. https://doi.org/10.2514/1.J060659.
[17] Tessitore N, Riccio A. A novel FEM model for biaxial non-crimp fabric composite materials under tension. Comput Struct 2006;84:1200–7. https://doi.org/10.1016/J.COMPSTRUC.2006.01.024.
[18] Arteiro A, Catalanotti G, Xavier J, Camanho PP. Notched response of non-crimp fabric thin-ply laminates. Compos Sci Technol 2013;79:97–114. https://doi.org/10.1016/j.compscitech.2013.02.001.
[19] Arteiro A, Catalanotti G, Xavier J, Camanho PP. Large damage capability of non-crimp fabric thin-ply laminates. Compos Part A Appl Sci Manuf 2014;63:110–22. https://doi.org/10.1016/j.compositesa.2014.04.002.
[20] Chomarat. C-Ply™ SP BX45 100 C3,4 12K HS n.d.
[21] Chomarat. C-Ply™ SP BX30 100 C3,4 12K HS n.d.
[22] ProSet. Technical Data, INF-114 INF-212, Infusion Epoxy 2021.
[23] 3M™. Scotch-Weld™EC-9323 B/A 2005.
[24] RenCast CW 2418-1 / Ren HY 5160 or HY 5161 or HY 5162 or HY 5118 datasheet 2012.
[25] ABAQUS/Standard User's Manual, Version 2021, Dassault Systmes Simulia Corp 2021.
[26] Hashin Z. Failure criteria for unidirectional fiber composites. J Appl Mech 1980;47:329–34. https://doi.org/10.1115/1.3153664.
[27] Benzeggagh ML, Kenane M. Measurement of mixed-mode delamination fracture toughness of unidirectional glass/epoxy composites with mixed-mode bending apparatus. Compos Sci Technol 1996;56:439–49. https://doi.org/10.1016/0266-3538(96)00005-X.
[28] Turon A, Dávila CG, Camanho PP, Costa J. An engineering solution for mesh size effects in the simulation of delamination using cohesive zone models. Eng Fract Mech 2007;74:1665–82. https://doi.org/10.1016/J.ENGFRACMECH.2006.08.025.
[29] Raimondo A, Doesburg SA, Bisagni C. Numerical study of quasi-static and fatigue delamination growth in a post-buckled composite stiffened panel. Compos Part B Eng 2020;182:107589. https://doi.org/10.1016/j.compositesb.2019.107589.
[30] van Dooren KS, Tijs BHAH, Waleson JEA, Bisagni C. Skin-stringer separation in post-buckling of butt-joint stiffened thermoplastic composite panels. Compos Struct 2023;304:116294. https://doi.org/10.1016/j.compstruct.2022.116294.
[31] Camanho PP, Maimí P, Dávila CG. Prediction of size effects in notched laminates using continuum damage mechanics. Compos Sci Technol 2007;67:2715–27. https://doi.org/10.1016/j.compscitech.2007.02.005.
[32] Santaniello M, Cestino E, Frulla G, Kruse-Strack T, Hallström S. Assessment of Defects Effect on Boltless Composites Longitudinal Joints. 2020.